buildings

MDPI

Article

Full-Scale Experimental Study on Flexural Performance of the New Precast UHPC Diaphragm Slab in Utility Tunnels

Quan Cheng [1], Zhengwei Li [2], Shaowei Deng [2], Haibo Jiang [1,*], Yueqiang Tian [3] and Jiayue Geng [1]

[1] School of Civil and Transportation Engineering, Guangdong University of Technology, Guangzhou 510006, China; 3117003038@mail2.gdut.edu.cn (Q.C.); 3221003263@mail2.gdut.edu.cn (J.G.)
[2] Guangzhou Communication Investment Urban Road Construction Co., Ltd., Guangzhou 510500, China; lizhengwei@mail.gjtjt.com (Z.L.); see464055019@163.com (S.D.)
[3] Zhonglu Xincai (Guangzhou) Technology Co., Ltd., Guangzhou 511430, China; tian_t4@126.com
* Correspondence: hbjiang@gdut.edu.cn

Abstract: In this paper, a bending test of a precast ultra-high-performance concrete (UHPC) diaphragm slab was carried out. The test revealed that the flexural failure process of specimens under the action of a positive bending moment can be divided into three stages: the elastic, crack-propagation, and yield stages. The first stiffness reduction of the structure was caused by cracks at the bottom of the diaphragm slab, while the second stiffness drop resulted from the yielding of the bottom longitudinal rebars. During the loading process, the ultimate bearing capacity was 3.75 times higher than the design load value (150 kN vs. 40 kN). Additionally, a nonlinear finite element model was established using Abaqus software validated by the test and exploiting parameter analysis. Based on this model, the initial crack stress of the actual slab was determined to be 5.12 MPa. Parameter analysis indicated that the shear strength of the diaphragm slab was stronger than the flexural strength, and the diaphragm slab's bearing capacity could be improved by increasing the ratio of bottom longitudinal reinforcement. This research confirmed that the new UHPC diaphragm slab used in Guangzhou Smart City is safe, and it also helped the design of similar UHPC slabs for utility tunnels.

Keywords: UHPC; utility tunnel; diaphragm slab; bending test; finite element simulation; parameter analysis

Citation: Cheng, Q.; Li, Z.; Deng, S.; Jiang, H.; Tian, Y.; Geng, J. Full-Scale Experimental Study on Flexural Performance of the New Precast UHPC Diaphragm Slab in Utility Tunnels. *Buildings* **2023**, *13*, 1349. https://doi.org/10.3390/buildings13051349

Academic Editor: Andreas Lampropoulos

Received: 22 April 2023
Revised: 12 May 2023
Accepted: 17 May 2023
Published: 22 May 2023

1. Introduction

1.1. Background

The term utility tunnel refers to the urban underground tube structure that contains the municipal pipelines of electric power, communications, radio and television, water supply, drainage, heat gas, etc. More than 147 cities in China will build utility tunnels to meet the growing demand of urban development in the coming decades [1]. The diaphragm slab plays an important role in separating the compartments and fixing pipelines in the utility tunnel. Usually, the diaphragm slab was made of conventional cast-in-place concrete, which had two critical disadvantages. One was the arrangement of supporting columns along the longitudinal direction of the utility tunnel, which occupied the limited internal space in the tunnel (Figure 1a). The other was that ordinary concrete slabs were subjected to cracking under the heavy load due to the low tensile strength of ordinary concrete. Cracking in concrete slabs can cause water leakage, which in turn may lead to the corrosion of reinforcing steel bars, particularly when cracks exceed a certain threshold width [2]. It would compromise the structural capacity, stiffness, and durability if they were not treated properly.

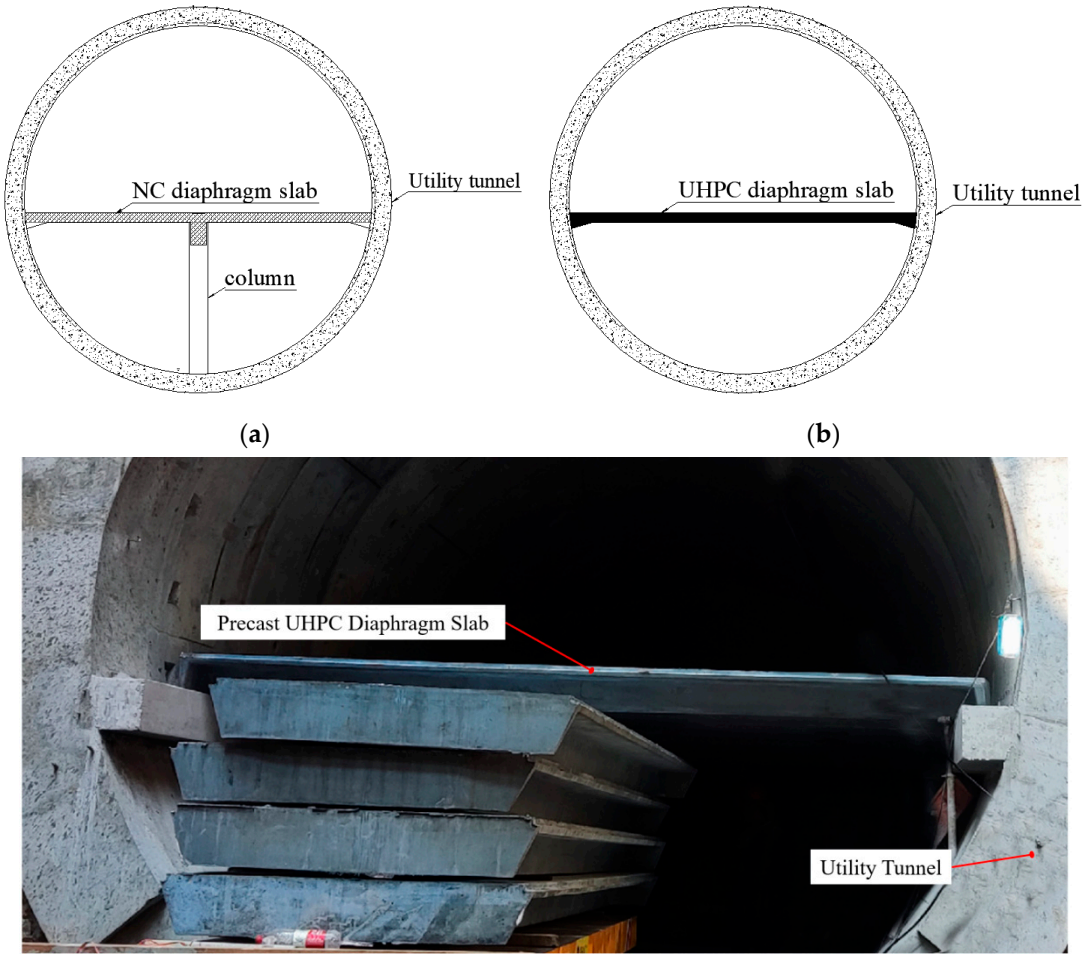

Figure 1. Schematic drawing of utility tunnels. (**a**) NC diaphragm slab, (**b**) ultra-high-performance concrete (UHPC) diaphragm slab, (**c**) Installation of precast UHPC diaphragm slab.

In contrast, precast structures offer numerous benefits, including increased efficiency, guaranteed quality, reduced labor requirements, and improved environmental sustainability. These advantages have been developed over the last 50 years and represent the future direction of the construction industry worldwide [3]. Many studies have been conducted on precast structures [4,5]. Additionally, ultra-high-performance concrete (UHPC) is an innovative cement-based composite, which consists of a cementitious component, Silica fume, quartz sand, a superplasticizer, and fibers [6,7]. It is considered one of the most promising construction materials for future sustainable infrastructure. The outstanding performance of UHPC has led many researchers to study various UHPC structures, such as steel-UHPC composite beams [8,9] and UHPC beams without stirrups [8–13]. Compared with conventional concrete, UHPC shows remarkable mechanical properties, fracture toughness, and high durability [14–16]. The compressive strength, modulus of elasticity, flexural strength, and tensile strength of UHPC are greater than 100 MPa [17], 40 GPa, 12 MPa, and 5 MPa, respectively [18]. With the incorporation of steel fibers (e.g., 2–3% by volume), UHPC obtains excellent tensile behavior with the propagation of multiple cracks [19]. UHPC with addition of steel fibers has been widely used in certain projects that require higher strength [20,21]. Combining the advantages of a precast structure and UHPC, the precast UHPC diaphragm slab (PUDS) can significantly increase the span of the slab, which eliminates the need for a middle support column and expedites the construction process. Additionally, the PUDS can mitigate the cracking issues that occur in cast-in-place ordinary concrete slabs under loads, temperature changes, shrinkage, and creep.

Recently, a new PUDS for utility tunnels has been applied in Guangzhou Smart City in China. Compared with the traditional cast-in-place normal concrete (NC) diaphragm slab (Figure 1a), the new precast UHPC slab used in the utility tunnel of Guangzhou Smart City has a lighter dead weight, larger span, better quality, better durability, more convenient construction and installation, and lower cost. Moreover, the absence of supporting columns increases the effective space of the utility tunnel (Figure 1b).

The PUDS can be treated as plate structures or beam structures. Several studies have been conducted on the UHPC plates and UHPC beams. Taking advantage of the excellent material properties of UHPC, Toutlemonde et al. took the lead in the innovative design of the UHPC rib and carried out experimental verification as well as preliminary analysis [22]. Aaleti and Ghasem have recently made considerable efforts to develop lightweight UHPC waffle deck panel systems [23,24]. Garcia performed the transverse flexural analysis of a UHPC two-way ribbed precast, prestressed bridge deck element [25]. Muhammad et al. further studied the flexural capacity of a single-rib UHPC T-slabs with four different reinforcing bar end anchoring methods [26]. Shao et al. conducted an experimental study on four UHPC short rib T-beams and conducted finite element analysis to explore the influence of the steel bar diameter, rib height, roof height, and transverse rib spacing on the bending performance of UHPC waffle slabs [27]. However, the above-mentioned UHPC slabs are mainly used for bridge decks.

To reveal the flexural performance of UHPC, many scholars have conducted in-depth research. Common conclusions were drawn. The increase of steel fiber content can improve the crack resistance of UHPC beams, with little effect on the ultimate load. Increasing the longitudinal reinforcement ratio can effectively improve the flexural capacity of UHPC beams [28]. The bending failure process of the UHPC reinforced beams can be divided into three stages, which are the elastic stage, crack-propagation stage, and yield stage from loading to failure [29]. When the beam is bending, many tightly spaced cracks formed perpendicular to the flexural tensile forces in the beam [30]. Peng put forward a calculation method for the flexural bearing capacity of the normal section of reinforced UHPC beams after research [31]. Zhu conducted further research on the flexural properties of UHPC T-beams through experiments [32].

1.2. Research Significance

In summary, the previous studies mainly focus on the UHPC slab used in bridges. To author's knowledge, few full-scale experimental studies have been conducted to investigate the mechanical properties of the UHPC diaphragm slabs used in utility tunnels.

The goal of this paper is to investigate the flexural and shear behaviors of the new precast UHPC diaphragm slab. To do this, a three-point bending full-scale test was conducted to explore the flexural performances and failure modes of this new UHPC slab. Additionally, a numerical model was developed to validate the experimental result. Due to the high cost of a full-scale test, the further research was completed with a numerical model. This model was used to investigate the shear behaviors and structural improvements. This research not only validated the safety of the new precast UHPC diaphragm slab used in Guangzhou Smart City, China but also provided reference for the design of actual UHPC precast diaphragm slabs in utility tunnels.

2. Experimental Program

2.1. Design and Description of Specimens

This full-scale slab was named UHPC-T-2475 and was made from UHPC. T indicated that the slab was investigated by tests, and 2475 represented the distance from the loading point to the fulcrums (units: mm). As shown in Figure 2, the total length of the test slab was 515 cm, and the clear span of the test slab was 495 cm after measuring the distance from the support to both ends of the beam. The top slab was 150 cm wide and 6 cm thick; the rib was 12 cm wide and 18 cm thick.

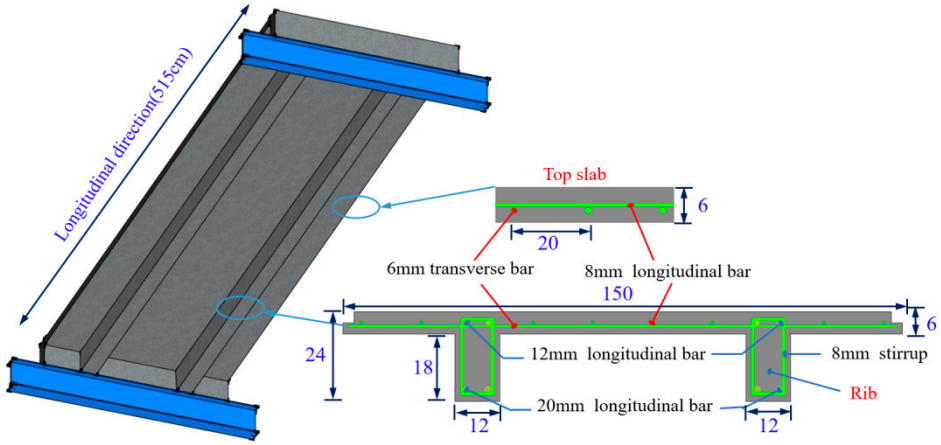

Figure 2. Structure details (units: cm).

2.2. Test Setup and Measurements

Loading Instruments

The loading device included a steel hinge, two load cells, two actuators and a reactive force frame, as shown in Figure 3. In the test, the test slab was laid on two supports. On one side was a roller support and on the other was a pin support. The pressure was applied by the actuator and transmitted to the test slab through the loading block. The magnitude of the pressure was measured by the load cell. The experimental set up was shown in Figure 4.

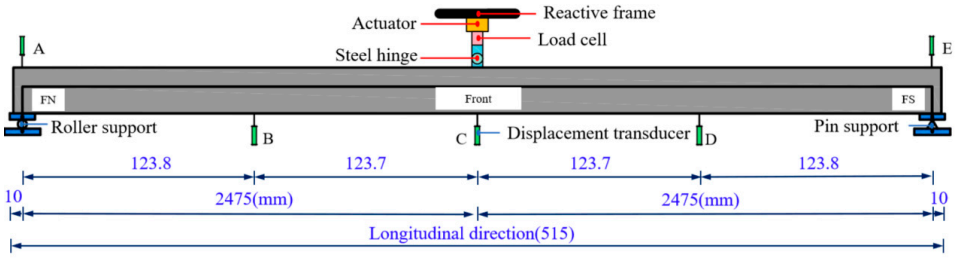

Figure 3. Sketch of experimental set up (units: cm).

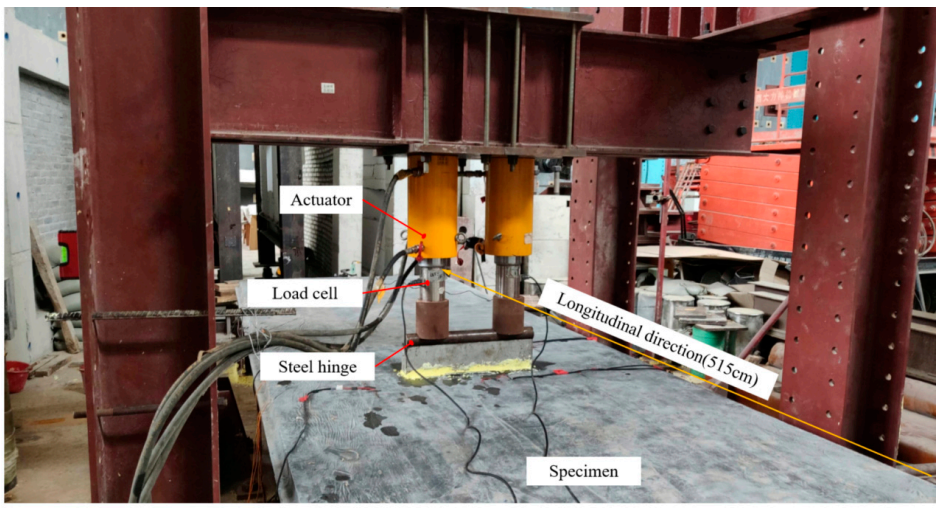

Figure 4. Photo of experimental set up.

2.3. Measurements

2.3.1. Displacement Measurements

According to the structural characteristics and combined with a comprehensive analysis, it was decided to measure the deflections of the beam at midspan, 1/4 span, and two supports, which was monitored by linear variable differential transformers (LVDTs). The arrangements of the deflection measuring points are shown in Figure 3. To distinguish directions, the specimen is divided into a N side and a S side on the shorter sides and front and back sides on the longer sides.

2.3.2. Strain Measurements

In order to obtain the strains of the test slab, six measuring points (a1, a2, a3, a4, a5, and a6) were arranged on the top surface of the test slab, two measuring points (a12 and a13) were arranged under the lower edge of the top slab, two measuring points (a10 and a11) were arranged under the side of the rib, and three measuring points (a7, a8 and a9) were arranged at the bottom of the rib, as shown in Figure 5. The strains of the concrete and steel bars were obtained with strain gauges.

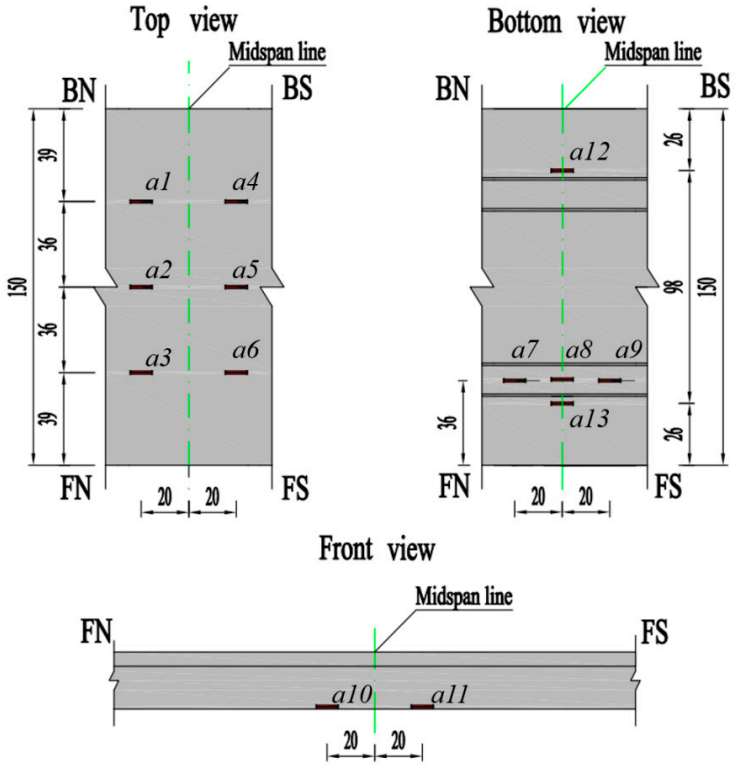

Figure 5. Arrangements of concrete strain gauges (units: cm). (BN represents the corner formed by the intersection of the north side and the back side. The other corner markers also have such directional meanings).

2.3.3. Loading Protocol

First, the specimen was preloaded to 10 kN, and the testing instruments were checked. The load gradually increased from 0 to 100 kN (75% of the calculated bearing capacity) in increments of 10 kN, and at each step, the experimental phenomena were observed, and data were recorded. Then, the loading process was controlled by displacement at increments of 2 mm until the failure of the specimen. During the loading process, the Jingming JM3813 multifunctional static collector was used to collect forces, strains, and displacements.

2.4. Material Properties

2.4.1. UHPC Properties

When pouring the test slab, three 100 mm × 100 mm × 100 mm prismatic specimens, three 100 mm × 100 mm × 400 mm prismatic specimens, and 100 mm × 100 mm × 300 mm cylindrical specimens were fabricated to measure the compressive strength, flexural strength, and elastic modulus, respectively. The test was carried out according to the method in the Chinese standard (MOHURD 2015) [33], and the mechanical properties of UHPC are listed in Table 1.

Table 1. UHPC properties.

Material	Properties	Parameter (MPa)
UHPC	Cubic compressive strength	141.0
	Flexural strength	18.5
	Elastic modulus	43,000

2.4.2. Steel Bars Properties

The steel bar tensile test was carried out according to the relevant Chinese production standards (SAMR, GB/T 1499.1492–2018) [34]. The obtained physical and mechanical properties of steel bars, such as yield strength and ultimate strength, are shown in Table 2.

Table 2. Steel bar properties.

Items	φ6 mm	φ8 mm	φ12 mm	φ20 mm
Yield strength (MPa)	448.6	461.6	469.2	425.8
Ultimate strength (MPa)	527.2	543.1	552.0	608.3
Elastic modulus (GPa)	189	190	198	195

3. Experimental Results and Discussions

3.1. Failure Modes

The failure mode of the test slab was a typical flexural failure. In the initial stage of loading, there was no crack in the bottom concrete, and the test slab was in the elastic stage. When the load reached 30 kN, the visible cracks appeared in the interior rib, and the test slab began to enter the crack-propagation stage. At this time, the stiffness began to decrease. With the loading continuously increased, a series of vertical cracks appeared in the bending section of the ribs. The rib was further cracked, and the cracks gradually extended upward. When the test slab was loaded to 130 kN, it entered the yield stage. At this stage, the bearing capacity increased slowly, but the stiffness decreased sharply and the deformation of the slab increased rapidly, with the bottom crack increasing. Finally, the experiment was terminated due to excessive deflection.

Figure 6 shows the failure pattern of the test slab at the ultimate load of 150 kN. It can be seen from the figure that when the test slab failed, there were still steel fibers connected at the cracks, and the test slab could still continue to deform and had good toughness.

Figure 6. Crack patterns.

3.2. Cracking Behaviors

When the test slab reached the cracking load, visible cracks appeared first in the rib at the bottom of the slab. There were only a few cracks under 40 kN load (design load). When loading to 80 kN, cracks extended to the middle of the rib. Cracks reached the top of the slab at 120 kN. Finally, vertical cracks expanded, and flexural failure occurred. The failure mode of experimental was shown in Figure 7.

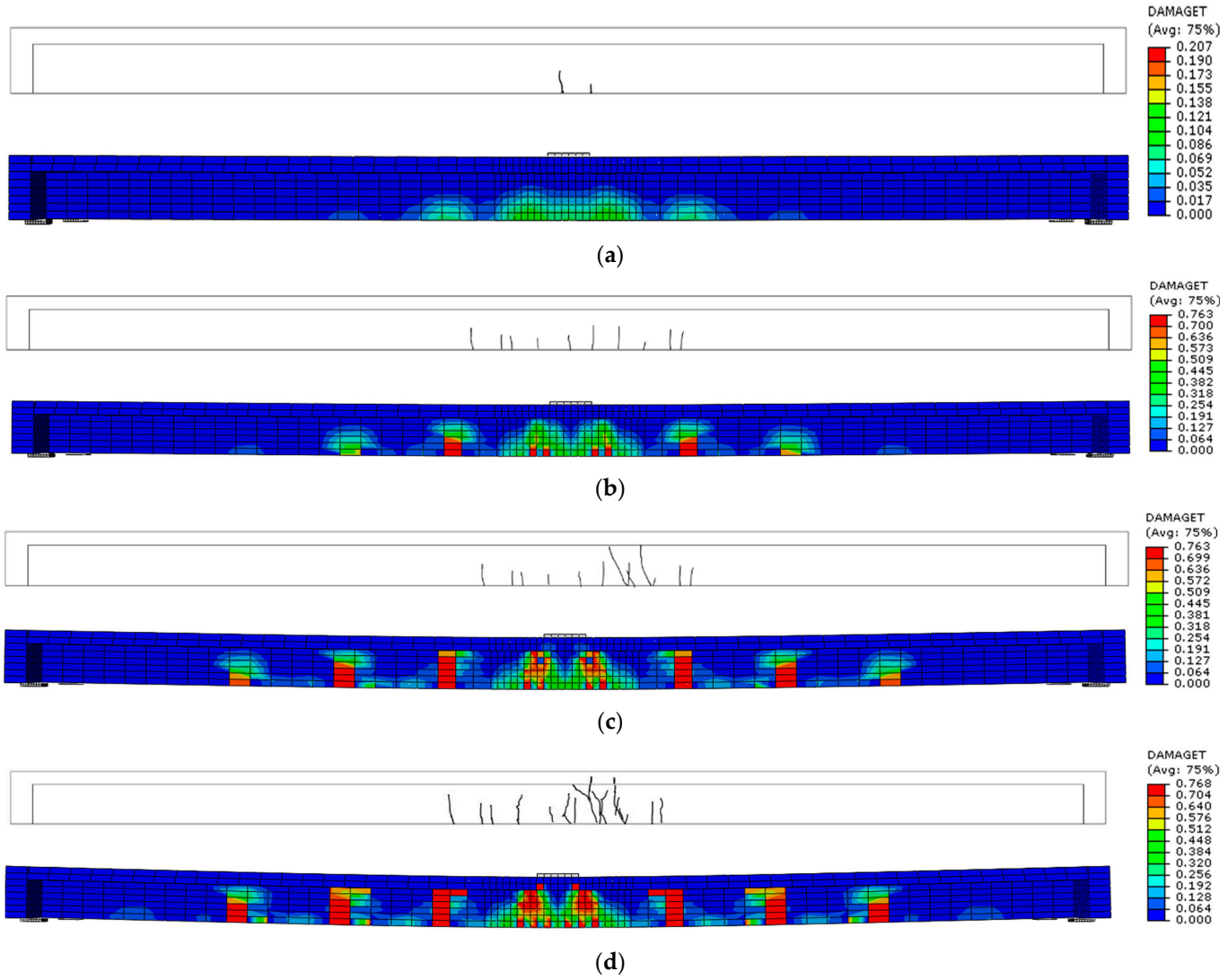

Figure 7. Failure mode of experimental and FE. (**a**) Cracking pattern of experimental and FE under 40 kN load (design load), (**b**) Cracking pattern of experimental and FE under 80 kN load (twice of design load), (**c**) Cracking pattern of experimental and FE under 120 kN load (three times of design load), (**d**) Cracking pattern of experimental and FE under 150 kN load (ultimate load).

4. Experimental Results and Discussions

4.1. Load–Deflection Behaviors

The mid-span deflection was calculated by $\delta = D_2 - (S_1 + S_2)/2$, where D_2 was the mid-span displacement, and S_1 and S_2 were the absolute values of the displacement at the support. The load-deflection curve was obtained from the flexural test, as shown in Figure 8, which indicated that the load-defection curve displayed three distinct stages. The first stage was the linear elastic stage, and the load-displacement curve was basically a linear straight segment, which indicated that the test slab was in the stage without cracks. Before the specimen was loaded to the cracking load (30 kN), the structural stiffness remained basically unchanged. Noticeable cracks were not observed in the UHPC. The second stage

was the crack-propagation stage. After the cracking load, with the increase of the load value, cracks initiated and propagated. The stiffness decreased, and the deflection grew faster, which indicated that the test slab had become elastoplastic due to the cracking of the slab. When the load reached 130 kN, the mid-span displacement gauge was about to reach its full-range, and it was removed. The slab approximately reached the ultimate load. The stiffness decreased further, the slab entered the yield stage, and the load slowly rose to the ultimate load (150 kN).

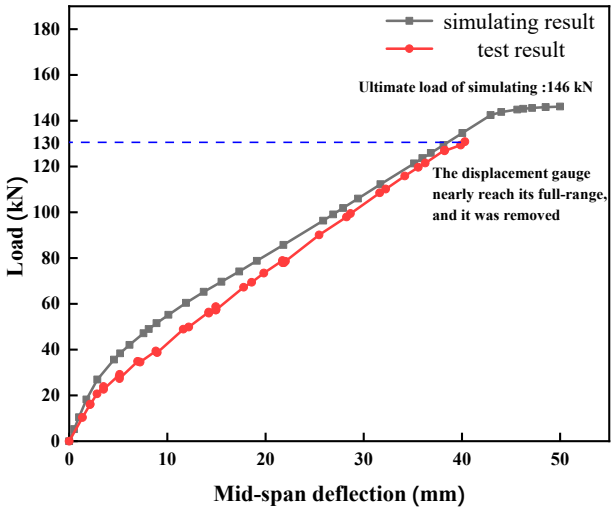

Figure 8. Load–deflection curve of mid-span.

Load–Strain Behaviors

Theoretically, the strain measuring points on the top of the pure bending section should have the same response. However, due to the randomness of concrete materials, the strain measured was different. From Figure 9a, it can be inferred that before the load value reached 130 kN, each measuring point at the top was in the linear scope, and the deviations were very small. While in the interval of 130 kN~150 kN, due to the expansion of the bottom crack, the section stiffness decreased, which can reflect the compressive strain of the measuring point, and the compressive strain increased rapidly.

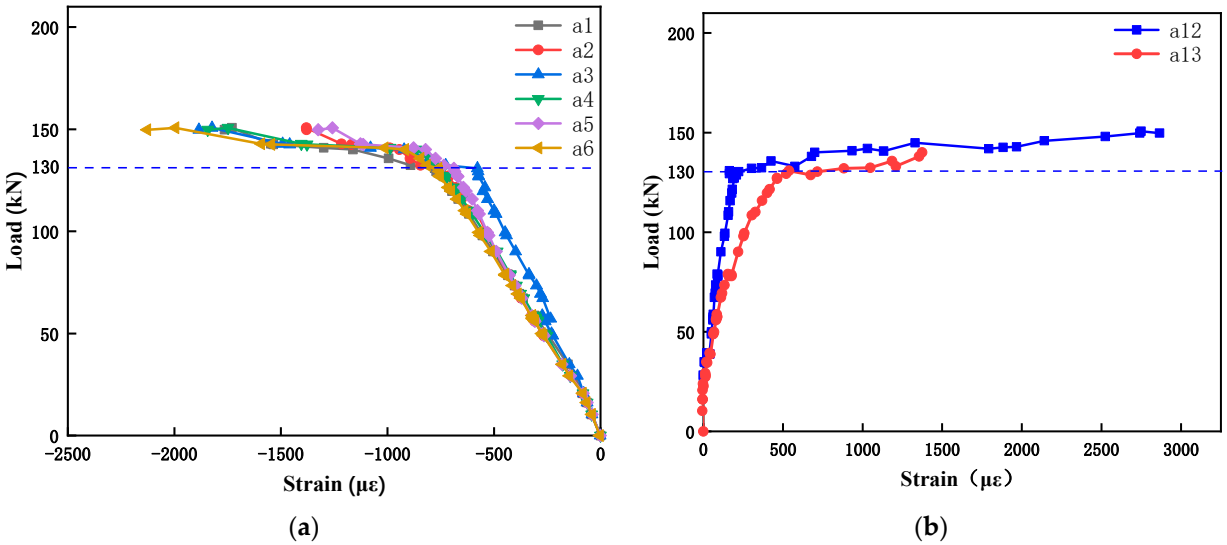

Figure 9. Load-strain curves at the top of the slab. (**a**) Load-strain curves on the top of the slab, (**b**) Load-strain curves under the lower edge of the top slab.

It can be seen from Figure 9b that before the load reached 30 kN (crack load), the strain at the bottom of the flange plate was close to zero, and the flange plate did not deform at this time. In the range of 30 kN~130 kN, the strains at the bottom of the flange plate and the overall load showed a linear relationship, which was consistent with the deformation trend of the slab top measuring point. When the load reached 130 kN, the cracks of the rib extended to the flange plate, and the strain increments of the flange plate were much larger than those in the elastic stage. Although the bending stiffness attenuated greatly, it still had load-bearing ability.

The load-strain relationship at the bottom of the slab was shown in Figure 10. When the load reached 20 kN, the strain measuring point at the bottom of the rib was damaged, due to the micro cracks that had begun to appear at this time. When the load reached 30 kN (visible crack load), there were visible cracks, and the strain gauges on the side of the rib were damaged.

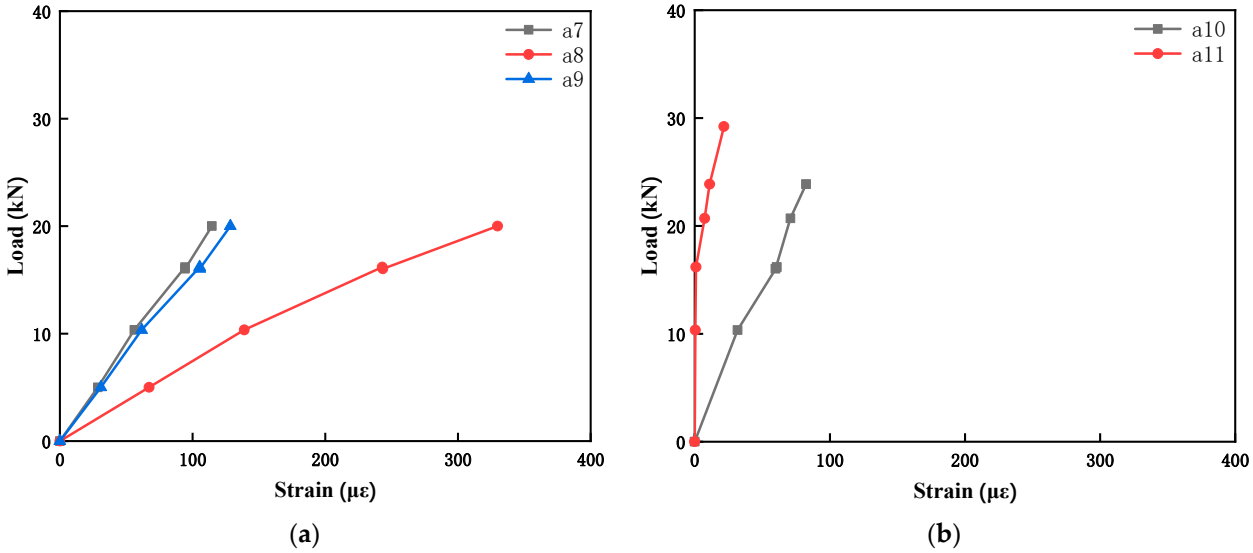

Figure 10. Load-strain curves at the bottom of the slab. (**a**) Load-strain curves under the side of the rib, (**b**) Load-strain curves under the rib.

4.2. Theoretical Calculation

4.2.1. Flexural Bearing Capacity

Considering the symmetry of the π-shape test slab, the section of the test slab was treated as two T-shaped sections. The ultimate bending moment of the UHPC-T beam was calculated utilizing the formula developed by Zhu et al. (2022) [32].

The characteristics of this T-shaped section conform to Formula (1). The neutral axis was in the flange, and the width of the rip was b. Considering the tensile effect of the UHPC in the tension zone of the web, the flexural bearing capacity of the normal section is calculated according to the following formulae:

$$f_y A_s + \beta f_{td} b(h - h_f) \leqslant \frac{1}{2} f_{cd} b_f h_f \tag{1}$$

$$M_u = \frac{1}{3} f_{cd} b_f x^2 + \frac{1}{2} \beta f_{td} b(h - x)^2 + f_y A_s (h_0 - x) + \frac{1}{2} \beta f_{td} (b_f - b)(h_f - x)^2 \tag{2}$$

The height of the UHPC compression zone should be calculated according to the following formula.

$$\frac{1}{2} f_{cd} b_f x = f_y A_s + \beta f_{td} b(h - x) + \beta f_{td} (b_f - b)(h_f - x) \tag{3}$$

β was the equivalent rectangular stress coefficient of UHPC in the tension zone; f_{cd} was the design value of the UHPC axial compressive strength; f_{td} was the UHPC axial tensile strength. A_s was the tensile steel bar total area; f_y was the yield strength of the steel bar. b was the width of the web; h_f was the height of the flange; h was the height of the section; h_0 was the effective height of the section; b_f was the width of the flange; and x was the height of the compression zone. The section of the single T-shaped section was shown in Figure 11.

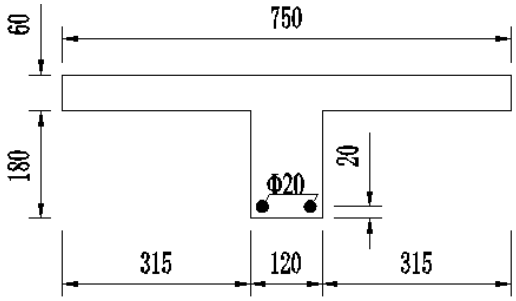

Figure 11. T-shaped sections.

The summary of calculation is shown in Table 3. The calculated flexural strength of the test slab with a single-rib T-slab was 77.4 kN·m according to Formula (2), and it indicated 154.9 kN·m for the π-shape. The converted mid-span corresponding load P_u^{c1} was 125.2 kN, and the reactive force at the support was 62.6 kN.

Table 3. The summary of calculated flexural strength.

Specimen Number	β	f_{cd} (MPa)	f_{td} (MPa)	b_f (mm)	A_s (mm)	f_y (MPa)	b (mm)	h_f (mm)	h (mm)	h_0 (mm)	x (mm)
UHPC-T-2475	0.9	135	6	750	628	400	120	60	240	220	8.6

4.2.2. Response 2000 Analysis

The material characteristics in Response 2000 were the same as those in the calculation of ultimate bearing capacity. The π-shaped section of the test slab was also regarded as two T-shaped sections for calculation purposes.

Through the running of Response 2000, the flexural strength of a single T-section was obtained as 78.7 kN·m. The flexural strength of the UHPC slab was twice of a single T-section section, which is 78.7 kN·m × 2 = 157.4 kN·m. The converted mid-span corresponding load P_u^{c2} was 127.2 kN, and the force V_u^{c2} was 63.6 kN.

4.2.3. Comparison of Calculation Results

Table 4 shows the comparison between the measured value and the calculated values of the flexural strength of the test slab. In this table, M_u is the measured ultimate flexural strength of the test plate, M_u^{c1} is the ultimate flexural strength of the test plate calculated according to Formula (2), M_u^{c2} is the ultimate flexural strength calculated by Response 2000, and M_u^{c3} is the ultimate flexural strength calculated in a later section by Abaqus. Comparing the experimental value and the calculated value, it can be seen that the ratio of the experimental value to the calculated value of Formula (2) is 1.19, the ratio of the experimental value to the calculated value of Response 2000 is 1.17, and the ratio of the experimental value to the Abaqus finite element calculation value is 1.02. All the calculated values are close to the experimental value.

Table 4. Comparison of calculation and test results.

Specimen Number	M_u/kN·m	M_u^{c1}/kN·m	M_u^{c2}/kN·m	M_u^{c3}/kN·m	$\frac{M_u}{M_u^{c1}}$	$\frac{M_u}{M_u^{c2}}$	$\frac{M_u}{M_u^{c3}}$
UHPC-T-2475	184.4	154.9	157.4	180.9	1.19	1.17	1.02

5. Numerical Analysis

5.1. The Abaqus Analysis

A finite element model (FEM) simulating the precast UHPC diaphragm slab was established with Abaqus software [35]. The concrete part was modeled with an eight-noded linear 3D brick solid element with reduced integration (C3D8R). The longitudinal reinforcement, erection reinforcement, and stirrup were modeled with two-noded linear 3D truss elements (T3D2), as the longitudinal and shear reinforcement bars only carry the axial forces. The grid of the middle failure section was dense, and the grids at both ends were sparse. The divided grid model is shown in Figure 12.

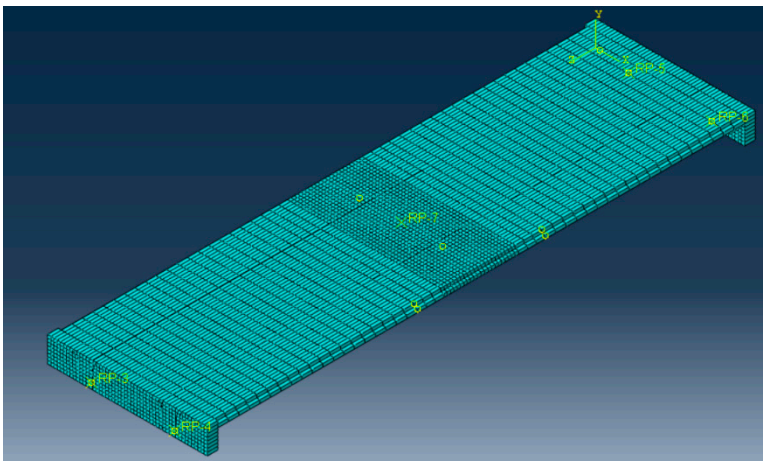

Figure 12. Mesh of simulated slab.

This paper mainly used the Concrete Damaged Plasticity (CDP) model to carry out the finite element analysis of concrete. This model was based on the damage model proposed by Lubliner, Lee, and Fenves (1998), which takes into account the difference in compressive and tensile properties of materials and assumes that the concrete material is mainly damaged by compressive crushing and tensile cracking [36,37]. In the Abaqus software, the Concrete Damaged Plasticity model required defining the plastic parameters of concrete (yield function, flow law, and other related parameters), as well as the relationship between tensile plasticity and damage and between compressive plasticity and damage. The parameter values of concrete in the CDP are shown in the following Table 5.

Table 5. Plastic properties of concrete.

Dilation Angle	Eccentricity	f_{b0}/f_{c0}	K	Viscosity Parameter
36°	0.1	1.16	0.667	0.005

Several studies investigated the behavior of UHPC material, such as that of Yin et al. (2017), who proposed a calibrated model for UHPC material [38]. In this study, the stress-

strain relationship curve given in Yang et al. (2008) [39] was used to describe the uniaxial compression behavior of concrete.

$$\sigma_c(\varepsilon) = \begin{cases} f_c \frac{n\xi - \xi^2}{1+(n-2)\xi} & \varepsilon \leqslant \varepsilon_0 \\ f_c \frac{\xi}{2(\xi-1)^2+\xi} & \varepsilon > \varepsilon_0 \end{cases} \quad (4)$$

f_c was the axial compressive strength of UHPC, which was 135 MPa; ε was the compressive strain of UHPC; σ_c was the tensile stress of UHPC; ε_0 was the peak strain of UHPC, which was 3500 με; $\xi = \varepsilon/\varepsilon_0$; $n = E_c/E_s$; E_c was the initial elastic modulus, taking E_c = 42.6 GPa; and E_s was the secant modulus at the peak point.

The tensile constitutive relation of UHPC was calculated with the bilinear stress-strain relation recommended in (Zhang et al., 2015) [40].

$$\sigma_t(\varepsilon) = \begin{cases} \frac{f_{ct}}{\varepsilon_{ca}}\varepsilon & 0 < \varepsilon \leqslant \varepsilon_{ca} \\ f_{ct} & \varepsilon_{ca} < \varepsilon \leqslant \varepsilon_{pc} \end{cases} \quad (5)$$

f_{ct} was the average stress in the stress-hardening stage, taking 6 MPa; ε_{ca} was the peak strain in the elastic stage, taking 199 με; ε_{pc} was the ultimate strain, taking 2000 με.

The steel bar used in the test slab was HRB400, which was selected according to the provisions in the literature [41], with the yield strength f_y = 400 MPa, the elastic modulus E_s = 200 GPa, and Poisson's ratio v_g = 0.3. The total elongation of the steel bar in tension and fracture should be not less than 7.5%.

The concrete slab and internal reinforcement were modeled separately. The reinforcing bars were composed of frame bars, stirrup bars, and longitudinal bars, which were embedded in the concrete slab with the embedded region command to simulate the reinforced concrete structure.

Reference points were set as constraint points at the support and the loading point, respectively. Supports were considered as a roller (U2 = U3 = 0) and a pin (U1 = U2 = U3 = 0), consistent with the experimental test.

5.2. Result of FEM Simulation

5.2.1. Load–Deflection Behaviors of the FE Model

In Figure 8, the black line was the simulated load-displacement curve, and the red line was the test load-displacement curve. The peak value P_u^{c3} from the FEM simulation was 146.2 kN (the bending moment M_u^{c3} was 180.9 kN·m), whereas the test peak load was 150 kN (accordingly, the bending moment was 184.4 kN·m) M_u/M_u^{c3} = 1.02. The ratio of the test peak load to the simulated peak load result was 1.02. Before the cracking load, the simulation results corresponded well with the actual test. After reaching the cracking load, the simulation results deviated. The stiffness of the simulated slab was higher than that of the UHPC test slab because of the ideal non-slip strong constraint between the steel bars and the concrete in FEMs. When loaded to 140 kN, the bottom longitudinal reinforcement stress reached 400 MPa.

To sum up, the calculations resulting from the finite element model were approximately consistent with the test results in the ultimate load, but there was a slight deviation in the stiffness.

5.2.2. Failure Mode

The red area shown in Figure 7 was the tensile damage area of the simulated slab. The failure modes of both the simulated slab and the test slab were the concrete cracking in the tension zone, and the cracks extended upward until failure. It can be seen that the main failure characteristics of the simulated slab were in good agreement with the experimental phenomena.

5.2.3. Initial Crack Stress Analysis

When the load of the precast UHPC slab was P = 30 kN, initial visible cracks appeared on the lower edge of the rib. According to the finite element calculation outputs, the cracking stress of the rib was 5.12 MPa.

5.3. Parametric Studies

After verifying the correctness of the FEM, parametric analysis was carried out on the specimens with different shear-span ratios to further reveal the structural behavior of the slab.

5.3.1. Shear Span Ratio

In order to explore the shear bearing capacity of the slab, three FEMs with shear-span ratios of 1.0, 2.0, and 3.0 were established. Shear span ratio $\lambda = a/h_0$, where a was the distance from the loading point to the fulcrum, and h_0 is the effective height of the section. The specific parameters are shown in Table 6. The schematic diagram of FEM loading is shown in Figure 13.

Table 6. Parametric Studies.

Specimen Number	*a* (mm)	*b* (mm)	h_0	λ
UHPC-N-220	220	4510	220	1.0
UHPC-N-440	440	4070	220	2.0
UHPC-N-660	660	3630	220	3.0

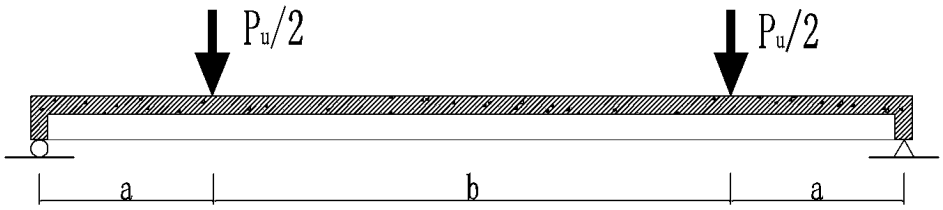

Figure 13. Schematic diagram of FEM loading.

5.3.2. Load–Deflection Behaviors with Different Shear-Span Ratio

V_u^{c4} was the support reaction force, and $V_u^{c4} = P_u^{c4}/2$ under four-point loading. It can be seen from Figure 14 that under different shear-span ratios, the slab was able to sustainably bear the load after the ultimate load. However, the ultimate load and the stiffness of the specimen increased with the decreasing of the shear-span ratios.

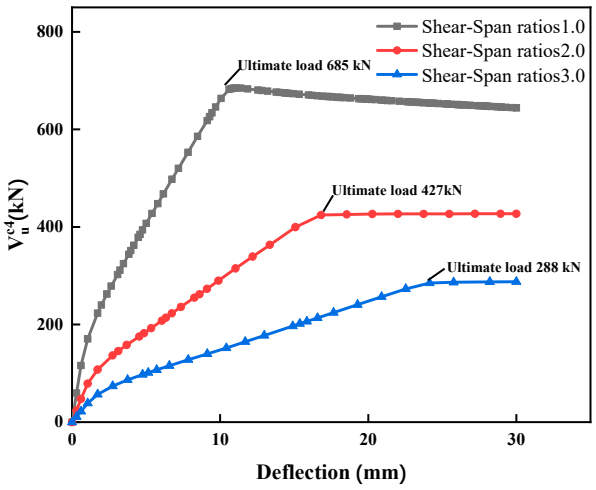

Figure 14. Load-deflection curves with different shear-span ratios.

5.3.3. Failure Modes with Different Shear-Span Ratios

The finite element simulation showed that under the shear-span ratio of 1.0, the concrete from the fulcrum to the supporting slab was crushed, and the stirrup yielded. The failure mode was shear failure. Under the shear-span ratio of 2.0 and 3.0, the concrete of the loading point and mid-span was damaged with the longitudinal bars yielding, which was the flexural damage (Figure 15).

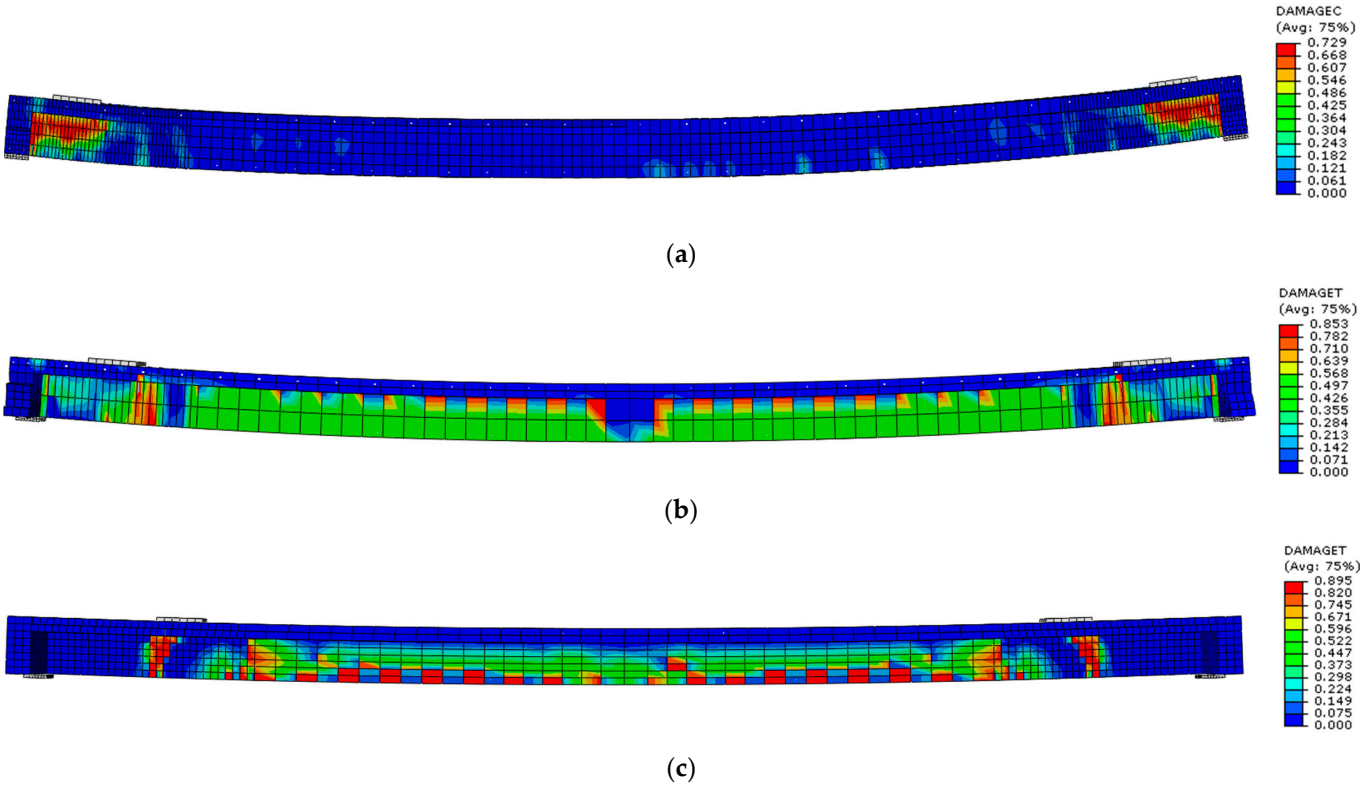

Figure 15. Failure mode with different shear-span ratios. (**a**) failure mode with shear-span ratio 1.0, (**b**) failure mode with shear-span ratio 2.0, (**c**) failure mode with shear-span ratio 3.0.

5.3.4. Calculation of Shear Capacity

The shear bearing capacity calculation method used was that in Article 6.2.1.1 of the French UHPC structural design code "NF P18-710-2016E" [42]. The calculation formula used the classical truss model to calculate the shear bearing capacity contribution V_c of the UHPC matrix and used the variable angle truss model to calculate the shear bearing capacity V_s of the stirrup, considering the contribution V_f of the steel fiber to the shear bearing capacity. The shear force calculation formula was as follows.

$$V_3 = V_c + V_s + V_f \tag{6}$$

$$V_c = \frac{0.21}{\gamma_{cf}\gamma_E} k_1 f_c^{\frac{1}{2}} bd \tag{7}$$

$$V_s = \frac{A_{sv}}{s} z f_y \cot(\theta) \tag{8}$$

$$V_f = A_b f_{cy} \cot(\theta) \tag{9}$$

V_c was the shear force contributed by the concrete; V_s was the shear force contributed by the stirrups; V_f was the shearing resistance of the steel fiber; γ_{cf} and γ_E are the design safety factors, taking γ_{cf} = 1.0, γ_E = 1.0 here; k_1 was the prestress influence coefficient,

taking as 1.0 for non-prestressing; A_{sv} was the cross-sectional area of stirrups; A_b was the effective cross-sectional area of the beam, and A_b took the cross-sectional area of the transverse rib of the slab; f_{cy} was the UHPC residual strength, and f_{cy} = 6.0 MPa. The calculation parameters and calculation results are shown in the above Table 7.

Table 7. Parameters and calculation results of shear bearing capacity.

b/mm	*z*/mm	*d*/mm	*S*/mm	A_{sv}/mm^2	A_b/mm^2	*θ*/°	f_y/MPa	f_{cy}/MPa	V_c/kN	V_s/kN	V_f/kN	V_3/kN
240	200	220	200	100.5	48,000	45	400	6	129	40	288	457

5.3.5. Comparison of Results

UHPC was the material of the simulated slab; N was numerical and the last number was the distance from the loading point to the support.

Table 8 presents a summary of the simulation and calculation results. V_u^{c4} was the maximum bearing section load of the numerical simulation; M_u^{c1} was the ultimate bending moment of the test slab calculated according to Formula (2); V_u^{c1} was the reactive load corresponding to the calculated ultimate bending bearing capacity. When the load point was concentrated, V_3 was the shear bearing capacity by Formula (6). After theoretical calculations, the ultimate bending moment of the test slab was 154.9 kN m, and the shear bearing capacity of the section was 457.0 kN.

Table 8. Summary of the simulating and calculation results.

Specimen Number	V_u^{c4}/kN	M_u^{c1}/kN·m	V_u^{c1}/kN	V_3/kN
UHPC-N-220	685.0	154.9	704.1	457.0
UHPC-N-440	427.2	154.9	352.0	457.0
UHPC-N-660	288.0	154.9	234.7	457.0

It can be seen from the above that when the shear-span ratio was 1.0, the maximum simulated supporting load of the specimen was V_u^{c4} = 685.1 kN, which was greater than the calculated shear bearing capacity of the section V_3 = 457.0 kN, and it was less than the reactive load V_u^{c1} = 704.1 kN, corresponding to the flexural strength of M_u^{c1} = 154.9 kN. Combined with Figure 16, it can be inferred that the failure mode was shear failure. When the shear span ratio was greater than 1.0, the shear resistance of the specimen was greater than the bending resistance, which illustrated flexural failure.

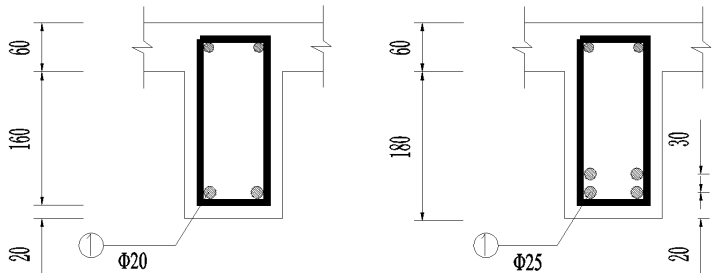

(**a**) (**b**)

Figure 16. Reinforcement diagram of Single T section. (**a**) Original reinforcement diagram of single T section. (**b**). Improved reinforcement diagram of single T section.

5.3.6. Design Suggestion

From the previous analysis, the shear resistance of the specimen was stronger than the bending resistance. When the shear-span ratio is greater than 1.0, the bending resistance of the specimen can be improved by increasing the longitudinal reinforcement ratio of the

transverse rib beam, which can fully exploit the material advantages of UHPC. Through finite element modeling, the reinforcement ratio of the bottom longitudinal reinforcement was increased to explore the ultimate flexural bearing capacity of the specimen. The reinforcement of the slab was shown in Figure 16; the specimen was loaded at three points according to Figure 4.

The reinforcement ratio was increased from 2.4% to 8.0%, and the ultimate bearing capacity increased from the original 150 kN to 270.6 kN. At the ultimate bearing capacity, the concrete at the bottom was broken and the longitudinal bars yielded, but the shear steel bars were in the elastic stage. From Figure 17, after the reinforcement ratio increased, the stiffness in the linear elastic stage was basically unchanged, while the stiffness increased in the crack stage, and the structural bearing capacity was significantly improved.

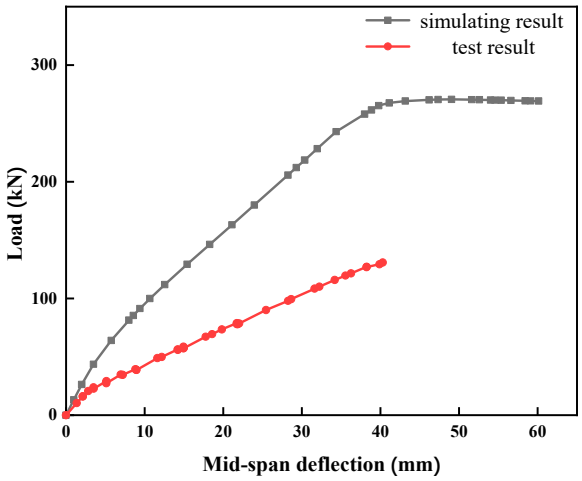

Figure 17. Load-deflection curves after increasing the reinforcement ratio.

6. Conclusions

In this paper, through a full-scale test study on the flexural performance of the new precast UHPC diaphragm slab, the cracking pattern, failure mode, ultimate bearing capacity, etc. were explored, and finite element models were established for further parameter analysis. The following can be obtained in conclusion.

(1) The UHPC slab showed excellent mechanical properties and deformation ability. Under the action of the design load of 40 kN, only some tiny cracks appeared in the rib, and the mid-span deflection was also small, being only 8.83 mm. This could ensure the normal service of the new slab in the tunnel.

(2) The entire process of flexural failure of the UHPC slab under three-point loading was divided into the elastic stage, the crack-propagation stage, and the yield stage. The ultimate bearing capacity (150 kN) of the specimen was 3.75 times the design load value (40 kN). Under the concentrated load in the mid-span, the failure mode of the slab was that the tensile steel bars at the bottom yielded, but the UHPC at the top was not crushed. The slab showed good toughness when it reached the ultimate load. Under the condition that the deflection increased sharply, it still conserved a high bearing capacity and no brittle failure occurred.

(3) Using the theoretical formula, Response 2000, and the Abaqus finite element model, the ultimate bearing capacity calculation results were 154.9 kN·m, 157.4 kN·m, and 180.9 kN·m, respectively. The ratio between the test value and the calculated values were 1.19, 1.17, and 1.02, respectively. The deviation between the calculated result and the test value was less than 20%. All the three calculation methods of flexural capacity can predict the flexural capacity of a slab accurately.

(4) The load-deflection curves and the failure modes obtained by the finite element model were in good agreement with the test results. The stress at the lower edge of the

rib during the initial crack test was 5.12 MPa. The parameter analysis of the finite element model showed that with the larger shear-span ratio, there is a smaller ultimate bearing capacity and lower stiffness of the specimen. The shear failure of the specimen occurred when the shear-span ratio was 1.0, but when the shear-span ratios were 2.0 and 3.0, flexural failure occurred. The French code formula can conservatively predict the shear capacity of slabs.

(5) In the finite element model, by increasing the reinforcement ratio of the bottom longitudinal reinforcement from 1.4% to 8.0%, the ultimate bearing capacity of the diaphragm slab can reach 270.6 kN, which was 1.8 times the existing test bearing capacity. The structural behaviors of the diaphragm slab made with the current design had a large room for improvement.

The objective of this paper was to investigate the flexural and shear behaviors of the new precast UHPC diaphragm slab and provide reference for the analysis and design of this new type of UHPC diaphragm slab. However, it should be noted that the findings of this study are only applicable to engineering as they are based on a single specimen and limited FEM parameter analysis. Additionally, the effect of the specific arrangement of the bottom longitudinal reinforcement and the reinforcement ratio on the mechanical properties of the UHPC diaphragm slab still need to be further studied by experiments.

Author Contributions: Conceptualization, H.J.; validation, J.G.; investigation, Q.C. and J.G.; resources, Y.T.; data curation, Q.C.; writing—original draft preparation, Q.C., Z.L. and S.D.; writing—review and editing, H.J.; visualization, Q.C.; supervision, H.J., Z.L., S.D. and Y.T.; project administration, H.J.; funding acquisition, H.J. All authors have read and agreed to the published version of the manuscript."

Funding: The research presented was funded by National Natural Science Foundation of China, grant number 51778150 (Study on shear failure mechanism and shear design theory of keyed joints in precast UHPC segmental beams; PI: Haibo Jiang).

Data Availability Statement: Not applicable.

Acknowledgments: The authors gratefully acknowledge the financial support of this work by the National Natural Science Foundation of China (51778150).

Conflicts of Interest: Authors do not have any conflict of interest.

References

1. Wang, T.; Tan, L.; Xie, S.; Ma, B. Development and applications of common utility tunnels in China. *Tunn. Undergr. Space Technol.* **2018**, *76*, 92–106. [CrossRef]
2. Pelà, A.L.; Aprile, A. Benedetti, Experimental study of retrofit solutions for damaged concrete bridge slabs. *Compos. Part B Eng.* **2012**, *43*, 2471–2479. [CrossRef]
3. Kurama, Y.C.; Sritharan, S.; Fleischman, R.B.; Restrepo, J.I.; Henry, R.S.; Cleland, N.M.; Ghosh, S.; Bonelli, P. Seismic-resistant precast concrete structures: State of the art. *J. Struct. Eng.* **2018**, *144*, 03118001. [CrossRef]
4. Cao, X.-Y.; Xiong, C.-Z.; Feng, D.-C.; Wu, G. Dynamic and probabilistic seismic performance assessment of precast prestressed reinforced concrete frames incorporating slab influence through three-dimensional spatial model. *Bull. Earthq. Eng.* **2022**, *20*, 6705–6739. [CrossRef]
5. Cao, X.-Y.; Feng, D.-C.; Wu, G.; Wang, Z. Experimental and theoretical investigations of the existing reinforced concrete frames retrofitted with the novel external SC-PBSPC BRBF sub-structures. *Eng. Struct.* **2022**, *256*, 113982. [CrossRef]
6. Shi, C.; Wu, Z.; Xiao, J.; Wang, D.; Huang, Z.; Fang, Z. A review on ultra high performance concrete: Part I. Raw materials and mixture design. *Constr. Build. Mater.* **2015**, *101*, 741–751. [CrossRef]
7. Ullah, R.; Qiang, Y.; Ahmad, J.; Vatin, N.I.; El-Shorbagy, M.A. Ultra-high-performance concrete (UHPC): A state-of-the-art review. *Materials* **2022**, *15*, 4131. [CrossRef]
8. Fang, S.; Zhang, S.; Cao, Z.; Zhao, G.; Fang, Z.; Ma, Y.; Jiang, H. Effects of stud aspect ratio and cover thickness on push-out performance of thin full-depth precast UHPC slabs with grouped short studs: Experimental evaluation and design considerations. *J. Build. Eng.* **2023**, *67*, 105910. [CrossRef]
9. Fang, Z.; Hu, L.; Jiang, H.; Fang, S.; Zhao, G.; Ma, Y. Shear performance of high-strength friction-grip bolted shear connector in prefabricated steel–UHPC composite beams: Finite element modelling and parametric study. *Case Stud. Constr. Mater.* **2023**, *18*, e01860. [CrossRef]
10. Feng, J.; Li, P.; Wu, J.; Jiang, H.; Tian, Y.; Sun, X. Shear behavior of externally prestressed UHPC beams without stirrups. *Case Stud. Constr. Mater.* **2023**, *18*, e01766. [CrossRef]

11. Jiang, H.; Huang, C.; Mei, G.; Gao, X.; Tian, Y.; Sun, X. Experimental and numerical investigations on direct shear performance of UHPC dry joints. *Eng. Struct.* **2023**, *283*, 115872. [CrossRef]
12. Jiang, H.; Hu, Z.; Cao, Z.; Gao, X.; Tian, Y.; Sun, X. Experimental and numerical study on shear performance of externally prestressed precast UHPC segmental beams without stirrups. In *Structures*; Elsevier: Amsterdam, The Netherlands, 2022; pp. 1134–1153.
13. Hu, Z.; Xu, Z.; Zhang, S.; Jiang, H.; Chen, Y.; Xiao, J. Experimental study on shear behavior of precast high-strength concrete segmental beams with external tendons and dry joints. *Buildings* **2022**, *12*, 134. [CrossRef]
14. Yu, Z.; Wu, L.; Yuan, Z.; Zhang, C.; Bangi, T. Mechanical properties, durability and application of ultra-high-performance concrete containing coarse aggregate (UHPC-CA): A review. *Constr. Build. Mater.* **2022**, *334*, 127360. [CrossRef]
15. Wu, L.-S.; Yu, Z.-H.; Zhang, C.; Bangi, T. Design approach, mechanical properties and cost-performance evaluation of ultra-high performance engineered cementitious composite (UHP-ECC): A review. *Constr. Build. Mater.* **2022**, *340*, 127734. [CrossRef]
16. Zhu, Y.; Zhang, Y.; Hussein, H.H.; Chen, G. Flexural strengthening of reinforced concrete beams or slabs using ultra-high performance concrete (UHPC): A state of the art review. *Eng. Struct.* **2020**, *205*, 110035. [CrossRef]
17. AFGC (French Association of Civil Engineering). *Ultra High Performance Fiber Reinforced Concrete Recommendations*; AFGC: Paris, France, 2013.
18. Yu, Z.; Wu, L.; Zhang, C.; Bangi, T. Influence of eco-friendly fine aggregate on macroscopic properties, microstructure and durability of ultra-high performance concrete: A review. *J. Build. Eng.* **2022**, *65*, 105783. [CrossRef]
19. Yoo, D.-Y.; Kang, S.-T.; Yoon, Y.-S. Enhancing the flexural performance of ultra-high-performance concrete using long steel fibers. *Compos. Struct.* **2016**, *147*, 220–230. [CrossRef]
20. Ragalwar, W.F.K.; Heard, B.A.; Williams, R. Ranade, Significance of the particle size distribution modulus for strain-hardening-ultra-high performance concrete (SH-UHPC) matrix design. *Constr. Build. Mater.* **2020**, *234*, 117423. [CrossRef]
21. Arora, A.; Almujaddidi, A.; Kianmofrad, F.; Mobasher, B.; Neithalath, N. Material design of economical ultra-high performance concrete (UHPC) and evaluation of their properties. *Cem. Concr. Compos.* **2019**, *104*, 103346. [CrossRef]
22. Toutlemonde, F.; Resplendino, J.; Sorelli, L.; Bouteille, S.; Brisard, S. Innovative design of ultra high-performance fiber reinforced concrete ribbed slab: Experimental validation and preliminary detailed analyses. In Proceedings of the 7th International Symposium on Utilization of High Strength/High Performance Concrete, Washington, DC, USA, 20–24 June 2005; pp. 1187–1206.
23. Aaleti, S.; Petersen, B.; Sritharan, S. *Design Guide for Precast UHPC Waffle Deck Panel System, Including Connections*; Federal Highway Administration: Washington, DC, USA, 2013.
24. Ghasemi, S.; Mirmiran, A.; Xiao, Y.; Mackie, K. Novel UHPC-CFRP waffle deck panel system for accelerated bridge construction. *J. Compos. Constr.* **2016**, *20*, 04015042. [CrossRef]
25. Garcia, H. *Analysis of an Ultra-High Performance Concrete Two-Way Ribbed Bridge Deck Slab*; Federal Highway Administration Office of Infrastructure: Washington, DC, USA, 2007.
26. Saleem, M.A.; Mirmiran, A.; Xia, J.; Mackie, K. Ultra-High-Performance Concrete Bridge Deck Reinforced with High-Strength Steel. *ACI Struct. J.* **2011**, *108*, 5.
27. Shao, X.; Li, Y.; Liao, Z.; Cao, J. Test and finite element analysis on bending performance of UHPC waffle deck panel. *J. Chang. Univ. (Nat. Sci. Ed.)* **2018**, *38*, 52–63.
28. Liang, X.; Wang, P.; Xu, M.; Wang, Z.; Yu, J.; Li, L. Investigation on flexural capacity of reinforced ultra high performance concrete beams. *Eng. Mech.* **2019**, *36*, 110–119. (In Chinese) [CrossRef]
29. Deng, Z.; Wang, Y.; Xiao, R.; Lan, M. Flexural test and theoretical analysis of UHPC beams with high strength rebars. *J. Basic Sci. Eng.* **2015**, *23*, 68–78. (In Chinese) [CrossRef]
30. Yang, I.H.; Joh, C.; Kim, B.-S. Structural behavior of ultra high performance concrete beams subjected to bending. *Eng. Struct.* **2010**, *32*, 3478–3487. [CrossRef]
31. Peng, F.; Fang, Z. Calculation approach for flexural capacity of reinforced UHPC beams. *China Civ. Eng. J.* **2021**, *54*, 86–97. (In Chinese) [CrossRef]
32. Zhu, Q.; Ye, L.; Cai, W.; Wen, X. Experimental study and theoretical calculations on flexural performance of UHPC-T beams. *J. Archit. Civ. Eng.* **2023**, *40*, 65–74. Available online: https://kns.cnki.net/kcms/detail/61.1442.TU.20220225.0946.004.html (accessed on 16 May 2023). (In Chinese).
33. *GB/T 31387-2015*; Reactive Powder Concrete. MOHURD (Ministry of Housing and Urban-Rural Development of the People's Republic of China): Beijing, China, 2015.
34. *GB/T 1499.1492-2018*; Steel for the Reinforcement of Concrete—Part 2: Hot Rolled Ribbed Bars. SAMR (State Administration for Market Regulation of the People's Republic of China): Beijing, China, 2018.
35. Duval, A.; Al-akhras, H.; Maurin, F.; Elguedj, T.; Duval, A.; Al-akhras, H.; Maurin, F.; Elguedj, T. *Abaqus/CAE 6.14 User's Manual*; Dassault Systémes Inc.: Velizy-Villacoublay, France, 2014.
36. Lubliner, J.; Oliver, J.; Oller, S.; Oñate, E. A plastic-damage model for concrete. *Int. J. Solids Struct.* **1989**, *25*, 299–326. [CrossRef]
37. Lee, J.; Fenves, G.L. Plastic-damage model for cyclic loading of concrete structures. *J. Eng. Mech.* **1998**, *124*, 892–900. [CrossRef]
38. Yin, H.; Shirai, K.; Teo, W. Numerical assessment of ultra-high performance concrete material. *IOP Conf. Ser. Mater. Sci. Eng.* **2017**, 012004. [CrossRef]
39. Yang, J.; Fang, Z. Research on stress-strain relation of ultra high performance concrete. *Concrete* **2008**, *225*, 11–15. (In Chinese)

40. Zhang, Z.; Shao, X.; Li, W.; Zhu, P. Axial tensile behavior test of ultra high performance concrete. *China J. Of. Highw. Transp.* **2015**, *28*, 50–58. (In Chinese) [CrossRef]
41. *GB 50010-2010*; Code for Design of Concrete Structures. MOHURD (Ministry of Housing and Urban-Rural Development of the People's Republic of China): Beijing, China, 2010.
42. Afnor, N.; Droll, K. *P18-710: National Addition to Eurocode 2—Design of Concrete Structures: Specific Rules for Ultra-High Performance Fiber-Reinforced Concrete (UHPFRC)*; Association Française de Normalisation: Saint-Denis, France, 2016.